PHILOSOPHICAL TRANSACTIONS OF THE ROYAL SOCIETY A MATHEMATICAL, PHYSICAL & ENGINEERING SCIENCES

Black Holes, Star Clusters, and Naked Singularities: Numerical Solution of Einstein's Equations

Stuart L. Shapiro and Saul A. Teukolsky

Phil. Trans. R. Soc. Lond. A 1992 **340**, 365-390
doi: 10.1098/rsta.1992.0073

Black holes, star clusters, and naked singularities: numerical solution of Einstein's equations

By Stuart L. Shapiro and Saul A. Teukolsky

Center for Radiophysics and Space Research, and Departments of Astronomy and Physics, Cornell University, Ithaca, New York, 14853, U.S.A.

We describe a new method for the numerical solution of Einstein's equations for the dynamical evolution of a *collisionless* gas of particles in general relativity. The gravitational field can be arbitrarily strong and particle velocities can approach the speed of light. The computational method uses the tools of numerical relativity and N-body particle simulation to follow the full nonlinear behaviour of these systems. Specifically, we solve the Vlasov equation in general relativity by particle simulation. The gravitational field is integrated by using the $3+1$ formalism of Arnowitt, Deser and Misner.

Physical applications include the stability of relativistic star clusters the binding energy criterion for stability, and the collapse of star clusters to black holes. Astrophysical issues addressed include the possible origin of quasars and active galactic nuclei via the collapse of dense star clusters to supermassive black holes.

The method described here also provides a new tool for studying the cosmic censorship hypothesis and the possibility of naked singularities. The formation of a naked singularity during the collapse of a finite object would pose a serious difficulty for the theory of general relativity. The hoop conjecture suggests that this possibility will never happen provided the object is sufficiently compact ($\lesssim M$) in all of its spatial dimensions. But what about the collapse of a long, non-rotating, prolate object to a thin spindle? Such collapse leads to a strong singularity in newtonian gravitation. Using our numerical code to evolve collisionless gas spheroids in full general relativity, we find that in all cases the spheroids collapse to singularities. When the spheroids are sufficiently compact the singularities are hidden inside black holes. However, when the spheroids are sufficiently large there are no apparent horizons. These results lend support to the hoop conjecture and appear to demonstrate that naked singularities can form in asymptotically flat space-times.

1. Introduction

Gravitational physics, like many other branches of nonlinear physics, has made significant advances with the advent of computers. Two areas of gravity research in particular have been the subject of intensive computational efforts in recent years. One area, loosely called 'N-body physics', is a variation of the classical N-body problem. Stripped to its bare essentials, this problem requires that a large number N of self-gravitating, but otherwise non-interacting, point particle masses be evolved numerically in time, starting from some given set of initial particle positions and velocities. The governing dynamical equation is Newton's law of motion in a many-

Phil. Trans. R. Soc. Lond. A (1992) **340**, 365–390
Printed in Great Britain

body, newtonian (Coulomb) gravitational field. The other area of intensive research is 'numerical relativity', a considerably younger pursuit. It concentrates on integrating forward in time on the computer the coupled Einstein equations of general relativity for the gravitational metric field and matter distribution, again starting from some well-posed initial data. Until recently, the matter distributions of interest have all been those of a fluid gas (and, typically, a perfect fluid) and are therefore controlled by the equations of relativistic hydrodynamics.

This paper is a review of our effort to link the two, heretofore distinct, computational endeavours described above. Specifically, we summarize highlights of numerical solutions of the Einstein equations for the dynamical evolution of a *collisionless* gas in general relativity. Our focus is on dynamical scenarios involving strong gravitational fields and high particle velocities approaching the speed of light. We thereby extend previous work on the N-body problem to the fully relativistic domain. We also extend previous work in numerical relativity to the régime of collisionless matter.

The analysis we present may casually be referred to as 'relativistic stellar dynamics on the computer'. Indeed, many of the key applications of our calculations address outstanding issues concerning the dynamical behaviour of relativistic star clusters. However, our results have far wider applicability, in that the matter fields need not be identified with stars *per se* but with any gas of collisionless, self-gravitating particles. It is more appropriate, then, to regard our computations very generally as numerical solutions of the collisionless Boltzmann (or Vlasov) equations for dynamical systems in general relativity.

The motivation for tackling this problem is at least threefold: computational, theoretical, and astrophysical. The primary computational goal is to learn how to solve Einstein's equations for interesting dynamical problems involving strong gravitational fields. Working with collisionless matter has several advantages over fluid systems for doing numerical relativity. The collisionless matter equations are ordinary differential equations (the geodesic equations), while hydrodynamical equations are partial differential equations. Furthermore, collisionless matter is not subject to shocks or other hydrodynamical discontinuities. These pathologies require special care in numerical simulations. Their absence allows one to focus all of the computational effort on solving Einstein's field equations. Consequently, the collisionless matter environment provides a golden opportunity to experiment with different numerical algorithms, coordinate choices, and so on. It is the Camelot for searching for the Holy Grail of numerical relativity – a code that simultaneously avoids singularities, handles black holes, maintains high accuracy, and runs forever.

Turning to the theoretical motivation, this work address several longstanding issues in relativistic stellar dynamics. Thus, for example, there exist as yet only sufficient, but not necessary, criteria for the radial stability of a spherical relativistic star cluster (Ipser 1980). Moreover, the nonlinear evolution and final fate of an unstable cluster had never been demonstrated before our study, although it had been conjectured (cf. Zel'dovich & Podurets 1965; Fackerell *et al.* 1969) that it was likely to be catastrophic collapse to a black hole. Previous work, based on perturbation theory (see §2), had been unable to resolve the stability issue completely and unable to address the issue of the fate at all. Fully nonlinear, time-dependent calculations were required to settle these important questions.

Because Einstein's equations are so difficult to solve analytically, numerical relativity is an important tool in resolving many fundamental issues that arise in the

PHILOSOPHICAL TRANSACTIONS OF THE ROYAL SOCIETY A MATHEMATICAL, PHYSICAL & ENGINEERING SCIENCES

theory. One such issue is the possibility that naked singularities might form from the collapse of well-behaved initial data. This would be a violation of Penrose's cosmic censorship hypothesis (Penrose 1969). Settling this question has defied analytic investigation for over 20 years. Hawking has called the issue 'the most important unsolved problem in classical general relativity'. As described below, recent collisionless matter simulations suggest that some limitations might be required to the unqualified cosmic censorship hypothesis.

Astrophysically, our study of the dynamical evolution of collisionless systems in general relativity has many potential applications in stellar dynamics, cosmology, and gravitational wave astronomy and some important associated observational consequences. It is amusing to recall that in the late 1960s and early 1970s, relativistic stellar dynamics was pursued in large measure to find gravitationally bound, high-redshift, stable systems to explain the high redshifts observed in quasars. Obviously, this particular pursuit is no longer very relevant today. However, explaining quasars and active galactic nuclei (AGNs) is still a burning issue. Lately it has become increasingly evident that quasars, AGNs, and other intense extragalactic radio sources are powered by jets of gas and magnetic fields and that each jet is produced by a compact supermassive object ($M \gtrsim 10^7 M_\odot$) in the nucleus of a galaxy (cf. Begelman *et al.* 1984). A supermassive black hole is the likely candidate for the compact object. But the puzzle remains: how and under what circumstances did these supermassive black holes form? Our numerical study of the collapse of relativistic stellar systems to supermassive black holes may provide some clues to this puzzle.

Non-spherical simulations of collisionless matter can address other important astrophysical topics, such as the generation of gravitational waves, and the collision of relativistic clusters and black holes. These phenomena will have to be understood if theorists are ever to decipher waveforms from the laser interferomer gravitational wave observatory now under construction.

If these are not reasons enough for studying relativistic stellar dynamics, we can always appeal to Authority:

> ... the collapse of a system of particles is very complicated. The problem is more difficult than the nonstationary hydrodynamical problem ... It is very desirable to perform calculations for such a model.
>
> (Zel'dovich & Podurets 1965)

2. Relativistic star clusters: historical perspective

The field of relativistic stellar dynamics was effectively launched by Einstein (1939), who constructed static, spherically symmetric, collisionless clusters of gravitating particles to investigate the physical significance of the Schwarzschild singularity. Einstein assumed that the particles all moved in circular orbits. He showed that $2GM/RC^2$, where M is the total mass-energy and R is the areal radius of a cluster, could never reach unity for such a system, so that the Schwarzschild singularity could never be realized.

(Einstein (1939) went on to infer that '"Schwarzschild singularities" do not exist in physical reality.... The "Schwarzschild singularity" does not appear for the reason that matter cannot be concentrated arbitrarily.' Although true for static, non-singular, equilibrium configurations, Einstein's statement is of course not true

for dynamic space-times, which can give rise to black holes and space-time singularities. See below for numerical demonstrations.)

Some years earlier, actually, Synge (1934) and Walker (1936) had laid the formal groundwork for more general discussions of collisionless distributions in relativity, while Walker derived the collisionless Boltzmann equation satisfied by the distribution function (see Fackerell (1968) for a slightly expanded summary of this early work).

For the most part, however, a casual perusal of the literature suggests that the field of relativistic stellar dynamics could have been named more aptly the study of relativistic stellar statics. That is, beginning with the spherical, circular orbit models of Einstein's (1939) (see also Zapolsky 1968), and extending through the more realistic, spherical, isotropic models of Zel'dovich & Podurets (1965), Fackerell (1968, 1970), Fackerell *et al.* (1969), Ipser & Thorne (1968), Ipser (1969*a*, *b*, 1980), Katz & Horwitz (1974), and Suffern & Fackerell (1976), previous work has focused on the construction of static solutions of collisionless systems in general relativity and the establishment of criteria for their stability (see Zel'dovich & Novikov (1971) Misner *et al.* (1973) for many more details and references). As noted in §1, much of this work was originally motivated by the discovery of quasars and the subsequent attempt to find intrinsically high redshift, stable, equilibrium systems to explain them. A number of interesting questions were raised in these studies. Can stable models with arbitrarily large redshifts be constructed? What are the perturbation equations for the radial deformation of spherical, equilibrium systems? Do there exist global stability criteria for the onset of gravitational collapse along equilibrium sequences of collisionless configurations, as is the case for fluid stars in general relativity? And so on.

A number of these intriguing questions were answered by these original investigations, which for the most part applied linear perturbation techniques to numerical models of spherical, equilibrium configurations. For example, following the suggestions by Zel'dovich & Podurets (1965) that sufficiently compact, high-redshift objects would be unstable to gravitational collapse, Ipser & Thorne (1968) formulated the theory of the stability of collisionless, spherical configurations against radial perturbations in the form of a variational principle. Ipser (1969*b*) then successfully reduced this variational principle to a form suitable for analysing, by use of trial functions, the radial stability of both isothermal and polytropic configurations, provided their equilibrium density distributions were not too centrally condensed. Fackerell (1970) extended this approach to study very centrally condensed clusters ('extreme core-halo configurations'). The upshot of this work was the numerical discovery that along a sequence of equilibrium configurations parametrized by z_c, the central redshift of the system, the onset of instability occurred very near the point of maximum fractional binding energy, $z_c \gtrsim 0.5$, independent of the nature of the models. The result was subsequently rigorized by Ipser (1980), who proved that appropriate one-parameter sequences of spherical, equilibrium configurations were stable at least up to the first maximum of the fractional binding energy.

Although appreciable progress was thus achieved in resolving some of the important issues, many of the key questions remained unsolved. For example, the inability to prove both a sufficient and necessary binding energy criterion for radial stability restricted the applicability of the binding energy curve as a stability diagnostic for collisionless systems. This contrasts with the situation for spherical

PHILOSOPHICAL TRANSACTIONS OF THE ROYAL SOCIETY A MATHEMATICAL, PHYSICAL & ENGINEERING SCIENCES

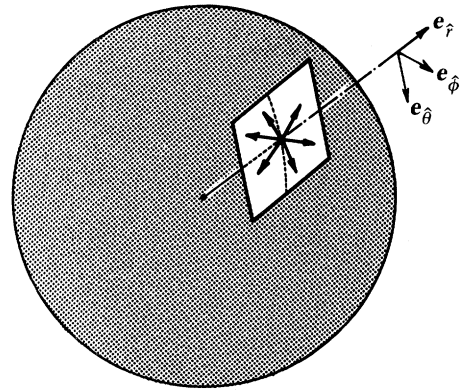

Figure 1. Schematic representation of the distribution of particles in a spherical star cluster.

fluid configurations (stars) in general relativity, for which the binding energy maximum rigorously locates the onset of radial instability. (Suffern & Fackerell (1976) concluded that in the case of a collisionless sequence, 'The confirmation or otherwise of this conjecture must await the development of more powerful methods for studying the dynamic stability of relativistic star clusters.') More significantly, the nonlinear evolution and ultimate fate of an unstable collisionless cluster could only be conjectured in these earlier studies.

Perhaps the most interesting and important concept to emerge from this previous work was the speculation, originally due to Zel'dovich & Podurets (1965), that unstable clusters inevitably undergo catastrophic collapse to a black hole (see also Fackerell *et al.* (1969) Zel'dovich & Novikov (1971) and Misner *et al.* (1973), who all subsequently endorsed this conjecture). Their qualitative scenario was recounted by Zel'dovich & Novikov (1971), who wrote,

> The physical picture of the collapse in this case is an increase of the core mass, accompanied by a transformation of formerly stable orbits into inward spirals, which lead the core and accompanying stars into their collective gravitational radius ... A numerical investigation of such collapse is badly needed, but no one up to now has had the fortitude to attempt it.

Part of the purpose of our study has been to muster the fortitude to examine many of the unresolved issues in relativistic stellar dynamics mentioned above.

3. Physical picture

Consider the situation in the simplest case, spherical symmetry. Imagine a sphere drawn in the interior of the collisionless matter distribution (figure 1).

The sphere is densely and uniformly covered with an infinite number of particles, each with infinitesimal rest mass. At any point on the sphere particles move in both the radial and transverse directions. To preserve spherical symmetry, we require that their motion be isotropic in the transverse plane. Thus, while individual particles may have finite angular momentum about the cluster centre, the total angular momentum summed over all the particles is zero.

The restriction to spherical symmetry reduces the number of phase space degrees

PHILOSOPHICAL TRANSACTIONS OF THE ROYAL SOCIETY A MATHEMATICAL, PHYSICAL & ENGINEERING SCIENCES

of freedom we have to keep track of. In coordinate space the only non-trivial dynamical variable is the radius r of a particle. In velocity space the non-trivial dynamical variables are the radial and transverse velocities, $u^{\hat{r}}$ and $u^{\hat{\perp}}$.

When we later generalize to axisymmetry, there are two non-trivial dynamical variables in coordinate space, r and θ, and three in velocity space, $u^{\hat{r}}$, $u^{\hat{\theta}}$, and $u^{\hat{\phi}}$.

4. Newtonian limit

Before considering the fully relativistic problem, it is instructive to examine how the spherical problem is solved in newtonian physics. For the motion of non-relativistic particles, the metric is just

$$ds^2 = -(1+2\Phi)\,dt^2 + dr^2 + r^2\,d\Omega^2, \tag{4.1}$$

where Φ is the newtonian potential. The matter moves according to the geodesic equations, which are simply Newton's Laws of Motion:

$$d\boldsymbol{x}/dt = \boldsymbol{u}, \quad d\boldsymbol{u}/dt = -\nabla\Phi, \tag{4.2}$$

where $\boldsymbol{x}$ and $\boldsymbol{u}$ are the position and velocity 3-vectors of each particle. Because of spherical symmetry, these equations simplify to

$$\left.\begin{aligned} dr/dt &= u_r, \\ du_r/dt &= -\Phi_{,r} + u_\phi^2/r^3, \\ u_\theta &= 0 \quad \text{(orbit confined to the plane } \theta = \tfrac{1}{2}\pi), \\ du_\phi/dt &= 0 \quad \text{(conservation of angular momentum).} \end{aligned}\right\} \tag{4.3}$$

These equations are integrated for every particle for a small timestep. The new particle positions then yield the rest-mass density ρ at the new time:

$$\rho = \sum_{\text{all particles}} mn, \tag{4.4}$$

where m is the particle rest mass and n the number density. The rest-mass density serves as the source term for the gravitational field equation, which in this case is simply Poisson's equation

$$\nabla^2\Phi = 4\pi G\rho. \tag{4.5}$$

Solving this equation gives the self-consistent gravitational field at the new time. The new potential is then inserted in the particle equations of motion and the process is repeated. This approach to evolving a self-gravitating, N-body system is known as a *mean-field, particle simulation scheme*.

5. Relativistic equations in spherical symmetry

Solving the relativistic problem in spherical symmetry is similar in spirit to the newtonian approach just described. A complete account is given in the series of papers by Shapiro & Teukolsky (1985*a*–*c*, 1986, hereafter Papers I–IV). A semi-popular treatment is given in Shapiro & Teukolsky (1988). The matter is evolved by N-body particle simulation and provides the source for the mean gravitational field, or metric. The metric is then determined by solving the ADM(3+1) equations

(Arnowitt *et al.* 1962). ADM cast the Einstein equations into a form suitable for evolving space-times into the future from well-posed initial data specified on a spacelike hypersurface. In this formulation of general relativity, four-dimensional space-time is split into (3+1)-dimensional space+time. This decomposition yields (1) 'constraint' or 'initial value' equations, which contain no time derivatives and relate field quantities (i.e. metric coefficients) on spacelike hypersurfaces; and (2) 'evolution' equations, which contain all the time derivatives and enable one to evolve field quantities from one time slice (i.e. spacelike hypersurface) to the next. (For an overview of the ADM formalism, see Misner *et al.* (1973) and Wald (1984).)

We adopt the isotropic form of the metric:

$$ds^2 = -(\alpha^2 - A^2\beta^2)\,dt^2 + 2A^2\beta\,dr\,dt + A^2(dr^2 + r^2\,d\theta^2 + r^2\sin^2\theta\,d\phi^2). \tag{5.1}$$

Here α and β are the lapse and shift functions of ADM. We use units with $c = G = 1$.

(*a*) *Matter equations*

The matter is described by the stress–energy tensor for a collisionless gas of particles,

$$T^{\mu\nu} = \sum_A m_A\, n_A\, u_A^\mu\, u_A^\nu. \tag{5.2}$$

Here m_A is the rest mass of particles of type A, u_A^μ is their 4-velocity, and n_A is their co-moving number density.

The equation of motion ($\nabla \cdot \boldsymbol{T} = 0$) for each particle is the geodesic equation

$$u^\mu_{;\nu}\, u^\nu = 0. \tag{5.3}$$

Once again these equations simplify in spherical symmetry, yielding

$$\left.\begin{aligned} dr/dt &= \alpha u_r/A^2(\alpha u^0) - \beta, \\ \frac{du_r}{dt} &= (\alpha u^0)\,\alpha_{,r} + u_r\beta_{,r} + \frac{\alpha u_r^2}{(\alpha u^0)}\frac{A_{,r}}{A^3} + \frac{\alpha u_\phi^2}{(\alpha u^0)}\left(\frac{1}{r^3A^2} + \frac{A_{,r}}{r^2A^3}\right), \\ u_\theta &= 0, \\ du_\phi/dt &= 0. \end{aligned}\right\} \tag{5.4}$$

The normalization of the 4-velocity,

$$u_\mu\, u^\mu = -1, \tag{5.5}$$

gives

$$\alpha u^0 = (1 + u_r^2/A^2 + u_\phi^2/r^2A^2)^{\frac{1}{2}}. \tag{5.6}$$

Thus, given the metric at any time t, equations (5.4) and (5.6) are integrated for the new positions and 4-velocities of the particles at $t + \Delta t$.

In the newtonian limit, $A \to 1$, $\alpha \to 1$, $\alpha_{,r} \to \Phi_{,r}$, $\beta \to 0$, and $u_0 \to 1$. We thus recover the newtonian equations of motion discussed in the previous section.

(*b*) *Source terms*

Given the particle positions and velocities, one can calculate the source terms needed in the field equations:

$$\left.\begin{aligned} \rho &= \sum_A m_A\, n_A(\alpha u_A^0)^2, \quad t_r = -\sum_A m_A\, n_A(\alpha u_A^0)\, u_{r(A)}, \\ T &= \sum_A m_A\, n_A, \quad S_{rr} = \sum_A m_A\, n_A u_{r(A)}\, u_{r(A)}. \end{aligned}\right\} \tag{5.7}$$

(c) *Field equations*

One of the challenges of numerical relativity is to find a good choice of coordinates so that one can actually solve the problem posed without encountering singularities. We have explored two choices of time coordinate. The first is the time coordinate defined by the *maximal slicing* condition. Mathematically, maximal slicing is defined by setting the trace of the extrinsic curvature of the $t = \text{const.}$ slices to zero:

$$\mathrm{Tr}\, K_{ij} \equiv K^i_i = 0. \tag{5.8}$$

Taking the trace of the evolution equation for $\partial_t K_{ij}$ then leads to an elliptic equation for the lapse function α, equation (5.15) below.

A different time-slicing condition has been proposed by D. M. Eardley (unpublished work) and by Bardeen & Piran (1983). This is the *polar slicing* condition: set the trace of the transverse part of K_{ij} to zero, that is, the part orthogonal to the radial direction. This can be written

$$K_{\mathrm{T}} \equiv K^\theta_\theta + K^\phi_\phi = 0. \tag{5.9}$$

The primary motivation for polar slicing was to find a coordinate condition that would make it easier to compute the amount of gravitational radiation emitted during non-spherical gravitational collapse. It was also hoped that this condition might have better singularity avoidance than maximal slicing when a black hole forms. This hope arises because polar slicing avoids regions of space-time containing trapped surfaces in spherical symmetry, and trapped surfaces signal the presence of an event horizon and the impending formation of a singularity. We have used our code to explore whether these expectations are actually met.

It is convenient to use the quantity K_{T} to write equations valid in both maximal and polar gauges:

$$K_{\mathrm{T}} = \begin{cases} 0, & \text{polar slicing,} \\ -K^r_r, & \text{maximal slicing.} \end{cases} \tag{5.10}$$

Then the evolution equation for the metric coefficient A is

$$A_{,t} = \beta(A_{,r} + A/r) - \tfrac{1}{2}\alpha A K_{\mathrm{T}}. \tag{5.11}$$

The hamiltonian constraint becomes

$$\frac{1}{r^2}\frac{\partial}{\partial r}\left(r^2 \frac{\partial}{\partial r} A^{\frac{1}{2}}\right) = -\tfrac{1}{4} A^{\frac{5}{2}}(8\pi\rho + \tfrac{3}{4}K_{\mathrm{T}}^2). \tag{5.12}$$

The shift β is given by the equation

$$\beta = -r\int_r^\infty \alpha(K^r_r - \tfrac{1}{2}K_{\mathrm{T}})\frac{\mathrm{d}r}{r}. \tag{5.13}$$

The momentum constraint determines the radial component of the extrinsic curvature:

$$K^r_r = \begin{cases} -\dfrac{8\pi}{A^3 r^3}\displaystyle\int_0^r A^3 r^3 t_r \,\mathrm{d}r, & \text{maximal,} \\ -\dfrac{4\pi r t_r}{1 + rA_{,r}/A}, & \text{polar.} \end{cases} \tag{5.14}$$

The lapse equation for maximal slicing is

$$\frac{\partial}{\partial r}\left(Ar^2\frac{\partial}{\partial r}\alpha\right) = \alpha A^3 r^2 [\tfrac{3}{2}(K^r_r)^2 + 8\pi\rho + 4\pi T], \tag{5.15}$$

while for polar slicing we get

$$\alpha = \frac{A_{\max}\alpha_{\max}}{A}\exp\left[\frac{1}{2}\int_{r_{\max}}^{r}\frac{r(A_{,r}/A)^2 + 8\pi r S_{rr}}{1 + rA_{,r}/A}\,\mathrm{d}r\right]. \tag{5.16}$$

(*d*) *Boundary conditions*

The boundary conditions on the metric variables are discussed in Paper I for maximal slicing and Paper IV for polar slicing. In brief, we match to asymptotic flatness at large r and impose regularity at the origin.

(*e*) *Diagnostics*

A number of self-consistency checks and diagnostic parameters for spherical systems are described in Papers I and IV. These include: conservation of the total mass-energy M; conservation of particle energy for stable, equilibrium clusters; null geodesic equations for light rays, used to map out the position of the event horizon; the criterion for the presence of trapped surfaces; and probes of the velocity distribution.

6. α-Freezing

Numerically, the above equations yield very accurate space-times for the most part. Examples will be shown below. However, as discussed in Paper IV, some of our integrations of collapsing clusters terminate well before the exterior space-time surrounding a growing, central black hole reaches a final stationary state. Thus it is not always possible for us to determine exactly what fraction of the total mass of a cluster ultimately forms a black hole and what fraction remains outside in orbit about the central hole. Not surprisingly, this problem is most severe when we evolve clusters with appreciable central concentration. Such configurations by construction are characterized by enormous dynamic range, with the dynamical (orbit) timescale in the central core significantly shorter than the dynamical timescale in the outer halo. Following the orbits of the central stars near the event horizon accurately on timescales sufficiently long to track the outer halo stars is crucial for determining the final fate of the configuration. This requirement imposes the ultimate limitation on the ability of our code to integrate arbitrarily far into the future.

Overcoming the above limitation is not merely of pedagogic interest. For as we discussed in Paper III (see §10 below), if relativistic star clusters do form in Nature, they are likely to be very centrally condensed. Moreover, the most interesting astrophysical scenarios – those that may be relevant to the birth of quasars and AGNs – involve the catastrophic collapse of extreme core-halo configurations with relativistic cores and extensive newtonian halos. These are precisely the clusters for which one would like to determine the final size of the black hole, but for which our original integrations, based on the equations of §5, had to terminate well before the evolution was completed.

Equally relevant, numerical problems encountered in evolving extreme core-halo spherical clusters often resemble problems that arise when trying to follow the propagation of gravitational waves during the evolution of non-spherical systems in

PHILOSOPHICAL TRANSACTIONS OF THE ROYAL SOCIETY A MATHEMATICAL, PHYSICAL & ENGINEERING SCIENCES

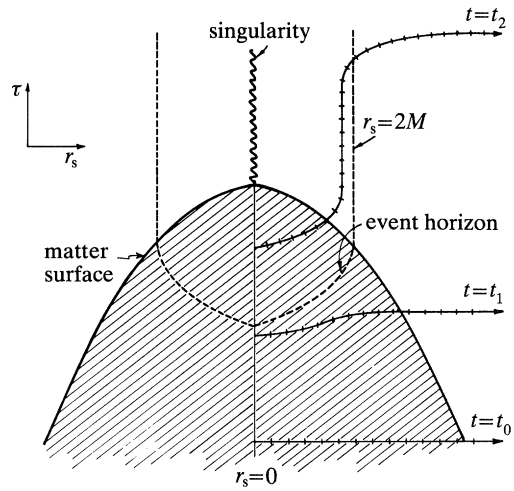

Figure 2. Schematic space-time diagram of the collapse of a star cluster to a black hole. The vertical axis is the proper time τ of particle worldlines, and the horizontal axis is areal (Schwarzschild) coordinate r_s. A singularity forms at the centre in a finite proper time. In a numerical calculation one chooses a time-slicing t that does not encounter the singularity by slowing down the advance of proper time near the centre. Shown are three time slices during the collapse. The tick marks on each slice represent a radial grid based on the isotropic coordinate r. When the spatial metric on the time slice t has the 'radial' form $A_s^2\,dr_s^2 + r_s^2\,d\Omega^2$, a spike develops in A_s near the event horizon, as in the usual static Schwarzschild geometry, even though no physical singularity is encountered. When the isotropic spatial metric $A^2\,dr^2 + A^2 r^2\,d\Omega^2$ is used, no spike appears. However, considerable radial grid must be expended along the throat near the horizon to accurately determine the metric there.

general relativity. In the latter situation, one must follow accurately the motion of matter near a black hole event horizon while simultaneously tracking the propagation of any radiation out to much larger radii. The complexity of this problem is also due, in part, to the vast dynamic range that characterizes a space-time with both a localized region of strong gravitational fields as well as a distant region with outgoing gravitational waves. Experience gained in solving the centrally condensed, spherical cluster problem may thus prove useful in the construction of reliable (2+1)- and (3+1)-dimensional numerical codes that can handle strong-field space-times with gravitational radiation.

Figure 2 illustrates the main effect responsible for our inability to track the late evolution of highly condensed clusters. Isotropic coordinates, while preventing 'spikes' from forming in the radial metric component near horizons (Smarr & York 1978), lead to considerable grid stretching all along the black hole throat. Grid stretching occurs because the isotropic radial coordinate r is forced to span many decades along the black hole throat. The metric field also varies rapidly on the throat. As a consequence, it is necessary to cover the throat with a growing number of grid points to determine the metric accurately in a numerical calculation. However, with the computational limitation of only a finite number of radial grid points available to cover the throat, the growing numerical inaccuracies induced by grid stretching ultimately force the integrations to terminate.

Furthermore, maximal time slicing, while successful in holding back the advance of proper time at the centre and thus postponing the formation of singularities, causes the lapse function α to decay and the spatial conformal factor A to increase

exponentially rapidly at late times at the centre. Thus underflows and overflows in the metric components may eventually accompany black hole formation, terminating the integrations before the exterior space-time reaches a final stationary state.

The unsatisfactory situation described above compels us to search for a better choice of space-time coordinates to solve the problem of centrally condensed spherical clusters.

Recall the physical meaning of the lapse function α: it gives the lapse of proper time $d\tau$ measured by an observer at rest in the t = const. hypersurfaces, for a given lapse of coordinate time dt:

$$d\tau = \alpha\, dt. \tag{6.1}$$

Such an observer is called a *normal* observer because his wordline is orthogonal to the t = const. hypersurface.

At late times during gravitational collapse, the lapse goes to zero exponentially with t near the centre of the configuration (the 'collapse of the lapse'; see Paper I for discussion and references). We therefore expect quantities measured by the normal observer there to freeze, or become constant with t at late times, because there is no lapse of proper time in the normal observer's reference frame.

As an example, consider the radial component of the velocity of a particle, $v^{\hat{r}}$, where the caret denotes a component measured by the normal observer. We have

$$v^{\hat{r}} = u^{\hat{r}}/u^{\hat{0}} = -\boldsymbol{u}\cdot\boldsymbol{e}_{\hat{r}}/\boldsymbol{u}\cdot\boldsymbol{e}_{\hat{0}}. \tag{6.2}$$

The time basis vector $\boldsymbol{e}_{\hat{0}}$ is just the 4-velocity of the normal observer, which is the unit normal $\boldsymbol{n}$ with components given by

$$n_\mu = (-\alpha, 0, 0, 0), \quad n^\mu = \alpha^{-1}\,(1, -\beta, 0, 0). \tag{6.3}$$

The radial basis vector is related to the coordinate radial basis vector by $\boldsymbol{e}_{\hat{r}} = \boldsymbol{e}_r/A$. Thus equation (6.2) becomes

$$v^{\hat{r}} = (u_r/A)/\alpha u^0. \tag{6.4}$$

Similarly

$$v^{\hat{\phi}} = (u_\phi/Ar)/\alpha u^0. \tag{6.5}$$

Substituting (6.4) and (6.5) in (5.6) gives

$$\alpha u^0 = [1-(v^{\hat{r}})^2-(v^{\hat{\phi}})^2]^{-\frac{1}{2}}. \tag{6.6}$$

Since $v^{\hat{r}}$ and $v^{\hat{\phi}}$ must freeze at late times, so must αu^0, and since u_ϕ is a constant of the motion, we see from (6.4) and (6.5) that the areal radius of a particle $r_s \equiv Ar$ and the quantity u_r/A also freeze.

It is straightforward to determine which quantities freeze and which do not as $\alpha \to 0$ (see Paper IV). In particular, as functions of r_s the source profiles ρ and T freeze, while t_r and S_{rr} do not. The quantities β, A, and r (isotropic radius of a particle) do not freeze. As a result, equation (5.4) shows that even when $\alpha \to 0$, the shift β continues to drive changes in r. This is the cause of grid stretching.

When α becomes small at late times near the centre of a collapsing configuration, it is customary in numerical work not to allow it to fall below some small value $\alpha_{\min}$ to avoid underflows. Since some quantities in the numerical evolution do get large, the question arises of exactly how small a value of $\alpha_{\min}$ is required. Having identified the variables that freeze, we note that cutting off α at $\alpha_{\min} \ll 1$ is entirely justified for equations involving those variables, but could be risky for variables that do not freeze.

Figure 3

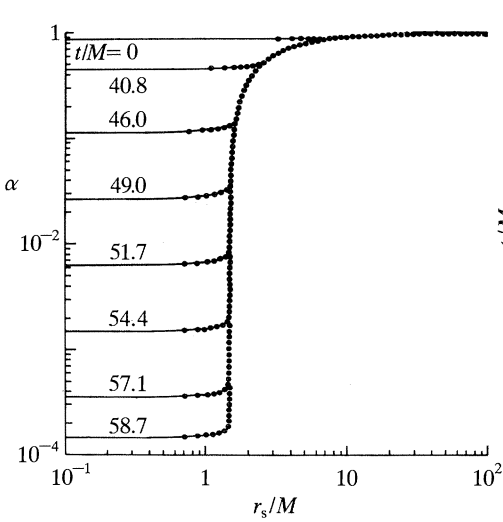

Figure 4

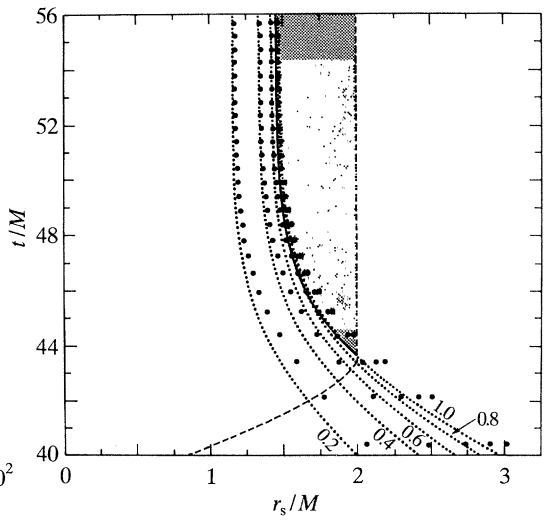

Figure 3. The lapse function α as a function of areal radius r_s on selected maximal time slices for Oppenheimer–Snyder collapse from $R = 10M$. —, Results of exact integrations by Petrich *et al.* (1985); ····, results obtained with the numerical code.

Figure 4. Space-time diagram for Oppenheimer–Snyder collapse in maximal slicing from $R = 10M$. The dotted lines are the worldlines of lagrangian matter elements from the exact integrations of Petrich *et al.* (1985). Each worldline is labelled by the fixed interior rest-mass fraction. The dots are points for the corresponding matter elements obtained with the numerical code. ----, Event horizon. The shaded area is the region of trapped surfaces. Its outer boundary, the apparent horizon, coincides with the event horizon. Its inner boundary is just inside the surface of the matter.

To overcome grid stretching and take advantage of α-freezing, we recast the equations in terms of the freezing variables. In either time slicing, the equations of motion of a particle become (Paper IV)

$$\frac{\mathrm{d}r_s}{\mathrm{d}t} = -\tfrac{1}{2}\alpha r_s K_T + \alpha \frac{u_r/A}{\alpha u^0} \Big/ \left(1 - \frac{r_s A_{,r_s}}{A}\right), \tag{6.7}$$

$$\frac{\mathrm{d}}{\mathrm{d}t}\left(\frac{u_r}{A}\right) = \left[-(\alpha u^0)\alpha_{,r_s} + \alpha \frac{u_\phi^2}{r_s^3(\alpha u^0)}\right] \Big/ \left(1 - \frac{r_s A_{,r_s}}{A}\right) + \alpha K_r^r \left(\frac{u_r}{A}\right). \tag{6.8}$$

Since every term on the right-hand sides of (6.7) and (6.8) contains an explicit α or $\alpha_{,r}$, we see that

$$\frac{\mathrm{d}r_s}{\mathrm{d}t} \to 0, \quad \frac{\mathrm{d}}{\mathrm{d}t}\left(\frac{u_r}{A}\right) \to 0 \quad \text{as} \quad \alpha \to 0. \tag{6.9}$$

This is a formal demonstration of the freezing of the particle motion at late times near the centre of a collapsing configuration in maximal or polar slicing.

For the detailed form of the field equations using freezing variables, see Paper IV.

7. Test-bed calculations

We have subjected our code to a rigorous and systematic battery of test-bed calculations. These tests not only served to identify bugs and instabilities, but also to

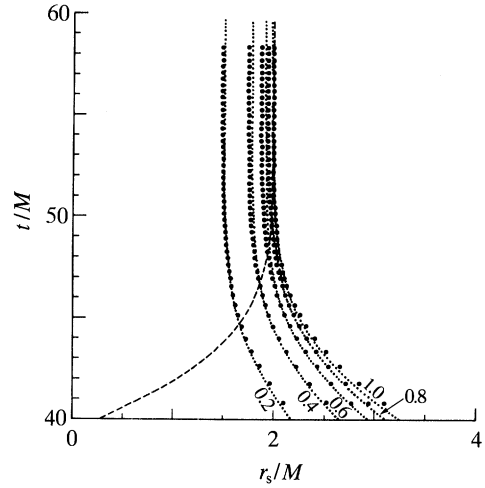

Figure 5. Space-time diagram for Oppenheimer–Snyder collapse in polar slicing from $R = 10M$. ····, Worldlines of lagrangian matter elements from the exact integrations of Petrich *et al.* (1986). Each worldline is labelled by the fixed interior rest-mass fractions. The dots are points for the corresponding matter elements obtained with the numerical code. ----, Event horizon.

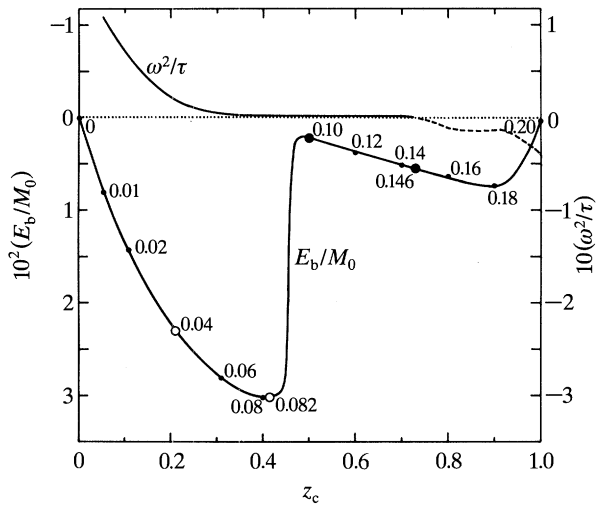

Figure 6. The $n = 4$ polytropic sequence. The fractional binding energy E_b/M_0 and oscillation frequency ω^2 in units of $\tau = \rho_c - P_c$ are plotted as functions of central redshift z_c. Clusters along the sequence are labelled by their value of the relativity parameter α as in Fackerell (1970). ○, Stable equilibrium; ●, collapse to a black hole.

root out inaccuracies and inefficiencies. In addition, they enabled us to calibrate the dynamic range of our code. The problem of dynamic range – the ability to handle problems where the variables span many decades – is particularly important because the applications most often encountered in Nature present exactly this difficulty.

We have performed 14 independent non-trivial tests. A full discussion of these tests is given in Papers I, II, and IV. As an example, consider the results for Oppenheimer–Synder collapse. Here we follow the collapse from rest of a homogeneous dust ball (initial areal radius $R/M = 10$) to a black hole. This is the

Figure 7

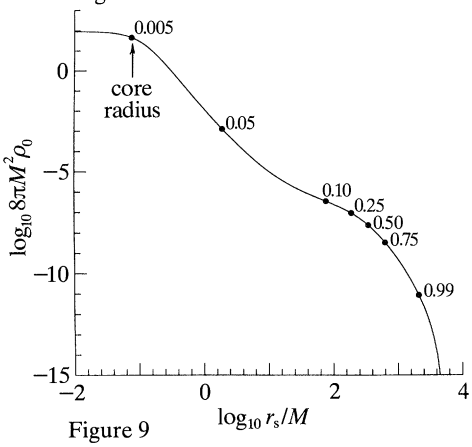

Figure 8

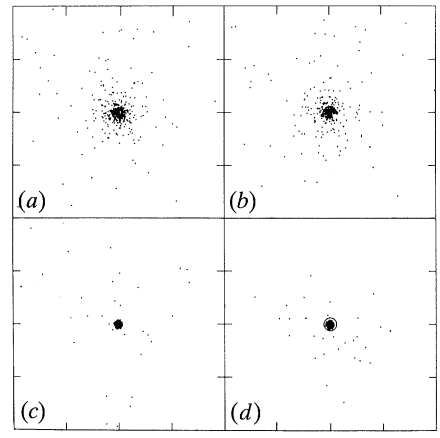

Figure 9

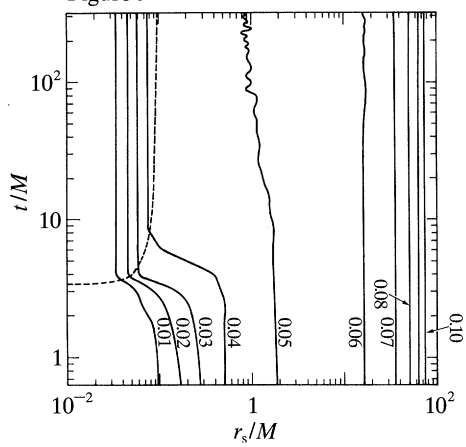

Figure 10

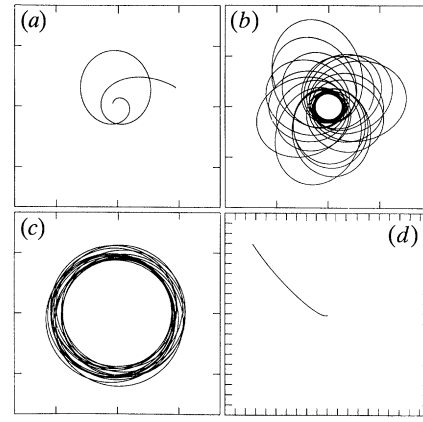

Figure 7. The initial rest-mass density profile ρ_0 for the relativistic polytrope with $n = 4$, $\Gamma = \frac{5}{4}$, and central redshift $z_c = 0.50$. The dots are located at points at which the interior rest-mass fraction has the values shown. This is an extreme core-halo configuration, with a highly relativistic core and an extensive newtonian halo. At the end of the evolution calculation the black hole contains a fraction 0.05 of the total rest mass, roughly 10 times the initial core mass.

Figure 8. Snapshots of the central regions $r_s/M \leqslant 2$ during the collapse of the extreme core-halo configuration shown in figure 7. The interval between radial grid markers is $\Delta r_s = 1\,M$. Here the collapse of the innermost regions to a black hole is evident. The circle in the last frame shows the event horizon at $r_s/M = 0.1$. Note that the cluster does not evolve appreciably after $t/M = 40$, but is characterized by the steady orbiting of stars about the central black hole. (*a*) $t/M = 0$, (*b*) $t/M = 2.38$, (*c*) $t/M = 40.53$, (*d*) $t/M = 439.80$.

Figure 9. Space-time diagram in polar slicing for the relativistic polytrope shown in figure 8. —, Worldlines of imaginary lagrangian matter tracers labelled by their fixed interior rest-mass fraction. ----, Event horizon. The event horizon asymptotes to $r_s/M = 0.1$, at which point it encompasses 5% of the total cluster rest mass.

Figure 10. Orbital trajectories of four typical particles near the cluster centre. Each particle N surrounds a fraction $N/7200$ of the total cluster rest mass at $t = 0$. In each frame the spacing between radial grid marks is $\Delta r_s = 1\,M$. In (*a*) the particle is initially in an elliptical-like orbit, but spirals in to the black hole after roughly two orbits. In (*b*) the particle moves in a nearly elliptical orbit, exhibiting large perihelion precision about the central black hole. Pericentre for this particle, $r_s/M = 0.25$, is one of the closest of all the particles that do not get captured, and remains stationary in time. In (*c*) the particle moves essentially unperturbed in a nearly circular orbit. In (*d*) the particle falls nearly radially into the black hole. (*a*) $N = 333$, (*b*) $N = 338$, (*c*) $N = 340$, (*d*) $N = 410$.

PHILOSOPHICAL TRANSACTIONS OF THE ROYAL SOCIETY A MATHEMATICAL, PHYSICAL & ENGINEERING SCIENCES

familiar Friedmann solution, which is known in closed analytic form in gaussian normal coordinates. For numerical comparisons, one must have available this solution in our coordinate system. The necessary transformations for both maximal and polar slicing have been carried out in Petrich *et al.* (1985, 1986).

In figure 3 we plot the lapse profile on selected maximal time slices during the collapse. The agreement between the exact and numerical solutions is very good, even after the black hole forms at $t/M \approx 40$.

In figure 4 we plot a space-time diagram for this case. The matter worldlines are accurately tracked by the numerical code. Moreover, the event horizon correctly appears at the origin, grows monotonically outwards, and remains stationary at $r_s/M = 2$ once the last particle crosses inside. Note that maximal time slicing manages to hold back the collapse and prevent the formation of a central singularity. However, it does not do so before the matter surface collapses well inside the horizon, to $r_s/M \approx 1.5$, and a region of trapped surfaces forms. This is in contrast to the situation shown in figure 5 for polar slicing. There the matter surface asymptotes to $r_s/M = 2$, and no trapped surface forms. This example nicely illustrates the stronger singularity avoidance property of polar slicing.

8. The stability of relativistic star clusters

As one important application of our code, consider the establishment of binding energy criteria for the stability of star clusters in general relativity. Imagine a sequence of equilibrium clusters each constructed from the same distribution function, but differing in central redshift z_c. Plot the fractional binding energy E_b/M_0 as a function of z_c along the sequence. Such a plot is shown in figure 6 for relativistic polytropes of index $n = 4$. Unlike the corresponding newtonian curve, which is monotonic, the relativistic binding energy curve has a turning point at sufficiently high redshift, $z_c \approx 0.5$. It is known that for a sequence of fluid equilibria, such a turning point signals the onset of radial instability. No such general theorem has been proven for collisionless equilibria (see Ipser & Thorne (1968), Ipser (1969*b*, 1980) and references therein for a discussion of previous work). We know from linear perturbation theory (utilizing trial functions in a variational principle) that at very high redshift the configurations are unstable. For some distribution functions, the point of instability appears to coincide with the binding energy maximum, to within numerical accuracy. However, as is clear from the figure, the onset of instability as determined by linear perturbation theory ($\omega^2 < 0$) occurs well beyond the turning point (Fackerell 1970). We do not know whether improved trial functions would show that instability actually sets in earlier along the sequence.

To find out what actually happens, we took models along the equilibrium sequence as initial data for our numerical code. Any numerical inaccuracies in the initial data or the evolution, however small, will induce collapse in an unstable configuration. As is evident from the figure, we find that all configurations beyond the first turning point are dynamically unstable. We thus conclude from this and other examples that the turning point on the binding energy curve does in fact signify the onset of dynamical instability. We therefore have 'discovered' a theorem awaiting a more formal proof.

Incidentally, the first unstable model shown in figure 6, with $z_c \approx 0.5$, is of particular interest. It is a prototype of an extreme core-halo configuration, containing

PHILOSOPHICAL TRANSACTIONS OF THE ROYAL SOCIETY A MATHEMATICAL, PHYSICAL & ENGINEERING SCIENCES

only 0.5% of its rest mass in a tiny relativistic core, and the remainder of the mass in an extensive newtonian halo, extending out to $R/M \approx 5000$. The ratio of the mean to central density is $\langle\rho\rangle/\rho_c = 4.0 \times 10^{-13}$. When this model collapses, a mass much larger than that of the core, approximately 5% of the rest mass, forms a central black hole. At the end of the collapse, the cluster settles in to a new stationary state consisting of a massive newtonian halo in orbit about a central black hole. This numerical example provides a viable scenario for the formation of a supermassive black hole in a galactic nucleus.

To handle this case we had to use the freezing version of our code, which was specially designed for configurations with such large dynamic range. Maximal slicing was not adequate to hold back the collapse. Before the cluster could settle into a final stationary state, the central lapse collapsed below $a_c \approx 10^{-70}$ and the central radial metric coefficient increased above $A_c \approx 10^{49}$. While α could be cut off below some minimum value $\alpha_{\min} \ll 1$ to avoid computer underflows, there is no way to cut off the growth of A and still maintain accuracy. Polar slicing in the freezing version proved adequate for this case, since A_c grows much more slowly with time in this gauge.

Several features of the collapse are highlighted in figures 7–10. The initial density profile is shown in figure 7. Snapshots of the central regions of the cluster inside $r_s/M = 2$ at selected times during the collapse are shown in figure 8. The cluster profile does not evolve significantly in the outer newtonian halo where most of the mass resides. However, the black hole is effective in 'sweeping clean' the innermost regions in and around the core. The cluster does not evolve much after $t/M = 40$ except for the steady orbiting of ambient stars about the central hole. The space-time diagram for the collapse is shown in figure 9.

The orbital trajectories of four typical particles near the cluster centre are plotted in figure 10. Interior to particle N at $t/M = 0$ resides a fraction $N/7200$ of the total cluster rest mass. Particle 333, which is initially in an elliptical-like orbit near $r_s/M = 1$, experiences inward spiral motion leading to capture by the black hole after two orbital periods. Particle 410 falls nearly radially from about $7M$ into the black hole. Particle 340 moves nearly unperturbed in a circular orbit at $1M$. Particle 338 moves in a nearly elliptical orbit extending out to $1.5M$ and exhibiting large perihelion precession about the central hole. Pericentre for this orbit appears to be one of the closest of all the ambient particles that do not get captured. It is located at $r_s/M = 0.25$ or $r_s/M_H \approx 5$. This is consistent with the fact that particles which orbit a stationary Schwarzschild black hole inside $r_s/M = 4$ are inevitably captured (see, for example, Misner *et al.* 1973). It is also satisfying that the pericentre position of this marginally stable orbit remains stationary with time, further confirming that by the time our integrations terminate, the cluster has achieved a new dynamic equilibrium about a stationary central black hole.

It has generally been believed that *all* relativistic clusters with central redshift $z_c \gtrsim 0.5$ should be dynamically unstable. The reason for this belief was that all the equilibrium sequences whose stability had been probed by linear perturbation theory satisfied this criterion (Ipser 1969*a*, *b*; Fackerell 1970). This belief has persisted in spite of speculations that some self-similar clusters with infinite central densities and redshifts constructed by Bisnovatyi-Kogan & Zel'dovich (1969) might be stable (see Bisnovatyi-Kogan & Thorne 1970). The unrealistic nature of these clusters made them appear of little interest. Moreover, all techniques for testing stability that were applied to them yielded inconclusive results.

Recently, finite, asymptotically flat clusters with arbitrarily large redshift have

PHILOSOPHICAL TRANSACTIONS OF THE ROYAL SOCIETY A MATHEMATICAL, PHYSICAL & ENGINEERING SCIENCES

been constructed by Kochanek *et al.* (1987). The fractional binding energy along a sequence of these clusters increases monotonically with central redshift. Therefore, according to the theorem of Ipser (1980), all clusters along the sequence should remain dynamically stable, even when their central redshifts become arbitrarily large. This behaviour has been confirmed by numerical simulations (Rasio *et al.* 1989*a*). These simulations used a novel technique for handling the matter, which is described in the next section. The principal conclusion of these studies is that binding energy, and not central redshift, provides the essential criterion for stability.

9. Direct solution of the Vlasov equation

The mean-field particle-simulation scheme discussed above provides particle positions and velocities, but does not provide the phase space distribution function f. Determining f requires the direct solution of the Vlasov equation in phase space. Very little effort has been devoted to this problem, even in newtonian gravity. An advantage of working with f is that the solution contains complete information on the matter distribution, and not merely the lowest moments.

We have recently developed a method to solve the relativistic Vlasov equation in spherical symmetry by exploiting Liouville's theorem (see Rasio *et al.* (1989*b*) for full discussion and references). The key idea for determining f at time t_2 knowing its value at t_1 is to implement the equation

$$f(x_2, v_2, t_2) = f(x_1, v_1, t_1),$$

where (x_1, v_1) is the position in phase space at time t_1 of a test particle that will reach the position (x_2, v_2) at time t_2. The gravitational field equations are of course the same as described above. The method accurately tracks the increasingly complicated fine-grained structure developed by the distribution function due to phase mixing. For moderate accuracies, the mean-field particle-simulation scheme is adequate. However, for high accuracy or for a detailed description of the phase space distribution, the direct method is superior.

10. The origin of quasars and AGNs

There is a wealth of evidence, albeit circumstantial, that supermassive black holes are the engines that power quasars and AGNs (see reviews by Rees (1984) and Begelman *et al.* (1984) and references therein for compelling arguments). Assuming that the black hole model is correct, it is straightforward to estimate the mass of the black hole. Such estimates typically give a range $10^6 \lesssim M/M_\odot \lesssim 10^9$. Even if the black hole hypothesis is correct, a key unanswered question remains: how and under what circumstances did such a supermassive black hole form?

Applying the result of our numerical simulations, we proposed in Paper III that the collapse of dense star clusters to supermassive black holes may provide the answer. Our scenario, which is similar to the original proposal of Zel'dovich & Podurets (1965), begins with a dense, but otherwise newtonian, cluster of compact stars – neutron stars or stellar mass black holes – residing at the centre of a galactic nucleus. Because of Coulomb scattering between the stars, the core of such a newtonian cluster inevitably undergoes a secular collapse on a relaxation timescale to a high density, high redshift state. Such secular newtonian collapse in a self-gravitating, large N-body stellar system is known as the *gravothermal catastrophe*, or simply *core collapse*. If core collapse should proceed all the way to a relativistic state, then the

PHILOSOPHICAL TRANSACTIONS OF THE ROYAL SOCIETY A MATHEMATICAL, PHYSICAL & ENGINEERING SCIENCES

resulting extreme core-halo configuration will be unstable to catastrophic collapse to a black hole. The collapse will take place rapidly, on a dynamical timescale. Our calculations show that those clusters capable of reaching such relativistic central redshifts in less than a Hubble time could possibly form supermassive black holes of precisely the right size to explain quasars and AGNs, $10^6 \lesssim M/M_\odot \lesssim 10^9$.

Gravitational radiation emitted in binary encounters can play an important role in this evolution (Quinlan & Shapiro 1987). A detailed treatment involving integration of the newtonian Fokker–Planck equation suggests that the original scenario, while leading to supermassive black holes, may be somewhat oversimplified (Quinlan & Shapiro 1989, 1990).

Ultimately, planned high-resolution Hubble Space Telescope observations of galactic nuclei may determine whether stellar conditions there are indeed suitable for triggering the black hole formation scenario we have proposed.

11. Non-spherical systems

Very little is known about non-spherical collisionless systems in relativity even for static equilibria. Dynamically, once we relax the restriction to spherical symmetry, two new facets can be explored: rotation and gravitational radiation. Our computations are the first to deal with these features numerically in the context of collisionless matter. A highlight of these investigations of space-times with collisionless matter is the ability to address fundamental issues in relativity like cosmic censorship and naked singularities.

(a) *Cosmic censorship, hoop conjecture, and naked singularities*

It is well known that general relativity admits solutions with singularities, and that such solutions can be produced by the gravitational collapse of non-singular, asymptotically flat initial data. The cosmic censorship hypothesis (Penrose 1969) states that such singularities will always be clothed by event horizons and hence can never be visible from the outside (no naked singularities). If cosmic censorship holds, then there is no problem with predicting the future evolution outside the event horizon. If it does not hold, then the formation of a naked singularity during collapse would be a disaster for general relativity theory. In this situation, one cannot say anything precise about the future evolution of any region of space containing the singularity since new information could emerge from it in a completely arbitrary way.

Are there guarantees that an event horizon will always hide a naked singularity? No definitive theorems exist. Proving the validity of cosmic censorship is perhaps the most outstanding problem in the theory of general relativity. Until recently, possible counter-examples (see, for example, Goldwirth *et al.* 1989) have all been restricted to spherical symmetry and typically involve shell crossing, shell focusing, or self-similarity. Are these singularities an accident of spherical symmetry?

Very little is known about non-spherical collapse in general relativity. In the absence of concrete theorems, Thorne (1972) has proposed the hoop conjecture: Black holes with horizons form when and only when a mass M gets compacted into a region whose circumference in every direction is $\mathscr{C} \lesssim 4\pi M$. If the hoop conjecture is correct, aspherical collapse with one or two dimensions appreciably larger than the others might then lead to naked singularities.

For example, consider the Lin–Mestel–Shu instability (Lin *et al.* 1965) for the

PHILOSOPHICAL TRANSACTIONS OF THE ROYAL SOCIETY A MATHEMATICAL, PHYSICAL & ENGINEERING SCIENCES

collapse of a non-rotating, homogeneous spheroid of collisionless matter in newtonian gravity. Such a configuration remains homogeneous and spheroidal during collapse. If the spheroid is slightly oblate, the configuration collapses to a pancake, while if the spheroid is slightly prolate, it collapses to a spindle. While in both cases the density becomes infinite, the formation of a spindle during prolate collapse is particularly worrisome. The gravitational potential, gravitational force, tidal force, kinetic and potential energies all blow up. This behaviour is far more serious than mere shell-crossing, where the density alone becomes momentarily infinite. For collisionless matter, prolate evolution is forced to terminate at the singular spindle state. For oblate evolution the matter simply passes through the pancake state, but then becomes prolate and also evolves to a spindle singularity.

Does this newtonian example have any relevance to general relativity? We already know that infinite cylinders do collapse to singularities in general relativity, and, in accord with the hoop conjecture, are not hidden by event horizons (Thorne 1972; Misner *et al.* 1973). But what about finite configurations in asymptotically flat space-times?

Previously, we constructed an analytic sequence of momentarily static, prolate and oblate collisionless spheroids in full general relativity (Nakamura *et al.* 1988). We found that in the limit of large eccentricity the solutions all become singular. In agreement with the hoop conjecture, extended spheroids have no apparent horizons. Can these singularities arise from the collapse of non-singular initial data? To answer this, we have performed fully relativistic dynamical calculations of the collapse of these spheroids, starting from non-singular initial configurations (Shapiro & Teukolsky 1991*a*, *b*).

We find that the collapse of a prolate spheroid with sufficiently large semi-major axis leads to a spindle singularity without an apparent horizon. Our numerical computations suggest that the hoop conjecture is valid, but that cosmic censorship does not hold because a naked singularity may form in non-spherical relativistic collapse.

(*b*) *Numerical code*

Our numerical code solves Einstein's equations for the evolution of non-rotating, collisionless matter in axisymmetric space-times. It is an extension of the treatment described above for spherical space-times and also of a newtonian method for axisymmetric configurations (Shapiro & Teukolsky 1987). It is designed to be able to handle cases in which the collisionless matter collapses to a singularity: specifically, oblate collapse to flat pancakes and prolate collapse to thin spindles.

We use maximal time slicing and isotropic spatial coordinates in axisymmetry. The metric is

$$\mathrm{d}s^2 = -\alpha^2\,\mathrm{d}t^2 + A^2(\mathrm{d}r + \beta^r\,\mathrm{d}t)^2 + A^2r^2(\mathrm{d}\theta + \beta^\theta\,\mathrm{d}t)^2 + B^2r^2\sin^2\theta\,\mathrm{d}\phi^2. \qquad (11.1)$$

We list the key equations in the Appendix.

We have carried out a large battery of test-bed calculations to ensure the reliability of the code. These tests included the propagation of linearized analytic quadrupole waves with and without matter sources and nonlinear Brill waves in vacuum space-times; maintaining equilibria and identifying the onset of instability for spherical equilibrium clusters (see above); reproducing Oppenheimer–Snyder collapse of homogeneous dust spheres and newtonian collapse of homogeneous spheroids (Lin *et al.* 1965; Shapiro & Teukolsky 1987). We constructed a number of geometric probes to diagnose the evolving space-time. We tracked the Brill mass and

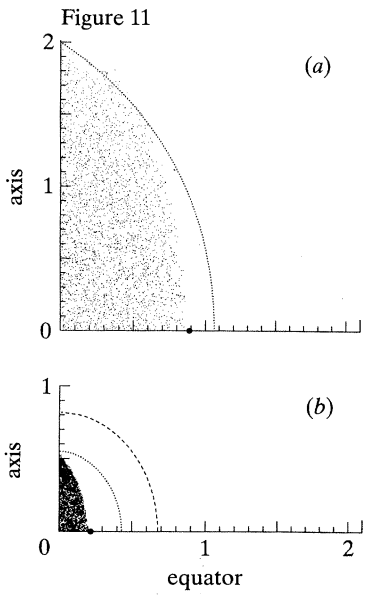

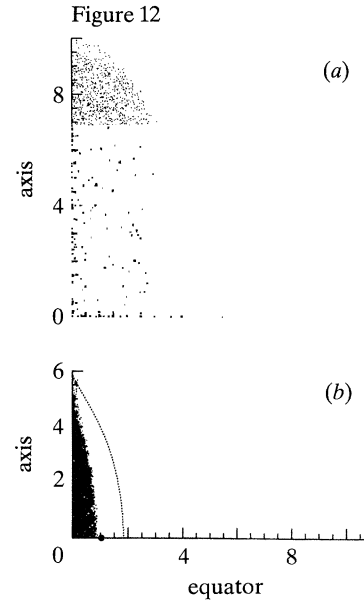

Figure 11. Snapshots of the particle positions at (*a*) initial ($t/M = 0$) and (*b*) late ($t/M = 7.7$) times for prolate collapse. The positions (in units of M) are projected onto a meridional plane. Initially the semi-major axis of the spheroid is $2M$ and the eccentricity is 0.9. The collapse proceeds non-homologously and terminates with the formation of a spindle singularity on the axis. However, an apparent horizon (dashed line) forms to cover the singularity. At $t/M = 7.7$ its area is $\mathscr{A}/16\pi M^2 = 0.98$, close to the asymptotic theoretical limit of 1. Its polar and equatorial circumferences at that time are $\mathscr{C}^{\rm AH}_{\rm pole}/4\pi M = 1.03$ and $\mathscr{C}^{\rm AH}_{\rm eq}/4\pi M = 0.91$. At later times these circumferences become equal and approach the expected theoretical value 1. The minimum exterior polar circumference is shown by a dotted line when it does not coincide with the matter surface. Likewise, the minimum equatorial circumference, which is a circle, is indicated by a solid dot. Here $\mathscr{C}^{\rm min}_{\rm eq}/4\pi M = 0.59$ and $\mathscr{C}^{\rm min}_{\rm pole}/4\pi M = 0.99$. The formation of a black hole is thus consistent with the hoop conjecture.

Figure 12. Snapshots of the particle positions at (*a*) the initial ($t/M = 0$) and (*b*) final ($t/M = 23$) times for prolate collapse with the same initial eccentricity as figure 11 but with initial semi-major axis equal to $10M$. The collapse proceeds as in figure 11, and terminates with the formation of a spindle singularity on the axis at $t/M = 23$. The minimum polar circumference is $\mathscr{C}^{\rm min}_{\rm pole}/4\pi M = 2.8$. There is no apparent horizon, in agreement with the hoop conjecture. This is a good candidate for a naked singularity, which would violate the cosmic censorship hypothesis.

outgoing radiation energy flux to monitor mass-energy conservation. To confirm the formation of a black hole, we probed the space-time for the appearance of an apparent horizon and computed its area and shape when it was present. To measure the growth of a singularity, we computed the Riemann invariant $I \equiv R_{\alpha\beta\gamma\delta}R^{\alpha\beta\gamma\delta}$ at every spatial grid point. To test the hoop conjecture, we computed the minimum equatorial and polar circumferences outside the matter.

Typical simulations were performed with a spatial grid of 100 radial and 32 angular zones, and with 6000 test particles. A key feature enabling us to snuggle close to singularities was that the angular grid could fan and the radial grid could contract to follow the matter.

(*c*) *Collapse of collisionless spheroids*

We followed the collapse of non-rotating prolate and oblate spheroids of various initial sizes and eccentricities. The matter particles are instantaneously at rest at $t = 0$ and the configurations give exact solutions of the relativistic initial-value

Figure 13

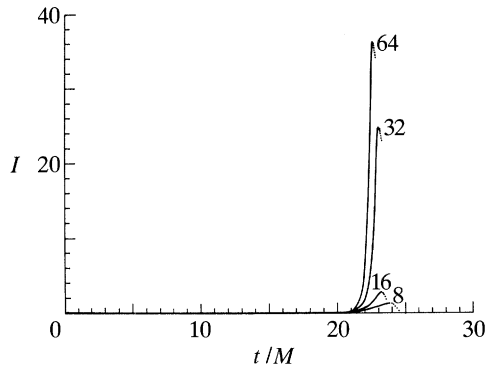

Figure 14

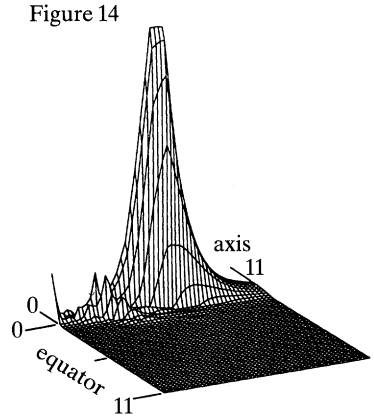

Figure 13. Growth of the Riemann invariant I (in units of M^{-4}) against time for the collapse shown in figure 12. The simulation was repeated with various angular grid resolutions. Each curve is labelled by the number of angular zones used. We use dots to show where the singularity has caused the code to become inaccurate.

Figure 14. Profile of I in a meridional plane for the collapse shown in figure 12. For the case of 32 angular zones shown here, the peak value of I is $24/M^4$ and occurs on the axis just outside the matter ($t/M = 23$).

equations (Nakamura *et al.* 1988). In the newtonian limit, these spheroids reduce to homogeneous spheroids. When they are large (size $\gg M$ in all directions) we confirm that their evolution is newtonian (Lin *et al.* 1965; Shapiro & Teukolsky 1987).

Figure 11 shows the fate of a typical prolate configuration that collapses from a highly compact and relativistic initial state to a black hole. Note that in isotropic coordinates a Schwarzschild black hole on the initial time slice would have radius $r = 0.5M$, corresponding to a Schwarzschild radius $r_s = 2M$. Figure 12 depicts the outcome of prolate collapse with the same initial eccentricity but from a larger semi-major axis. Here the configuration collapses to a spindle singularity at the pole without the appearance of any apparent horizon. (We searched for both a single global horizon centred on the origin as well as a small disjoint horizon around the singularity in each hemisphere.) The spindle consists of a concentration of matter near the axis at $r \approx 5M$. Figure 13 shows the growth of the Riemann invariant I at $r = 6.1M$ on the axis, just outside the matter. Before the formation of the singularity, the typical size of I at any exterior radius r on the axis is about $M^2/r^6 \ll 1$. With the formation of the spindle singularity, the value of I rises without bound in the region near the pole. The maximum value of I determined by our code is limited only by the resolution of the angular grid: the better we resolve the spindle the larger the value of I we can attain before the singularity causes the code (and space-time!) to break down. Unlike shell-crossing singularities, where I blows up in the matter interior whenever the matter density is momentarily infinite, the singularity also extends outside the matter beyond the pole at $r = 5.8M$ (figure 14). In fact, the peak value of I occurs in the vacuum at $r \approx 6.1M$. Here the exterior tidal gravitational field is blowing up, which is not the case for shell crossing. The absence of an apparent horizon suggests that the spindle is a naked singularity.

When our simulation terminates, I along the axis falls to half its peak value at $r \approx 4.5M$ inside the matter and $r \approx 6.7M$ outside the matter. The singularity is not a point. Rather it is an extended region which includes the matter spindle, but grows

PHILOSOPHICAL TRANSACTIONS OF THE ROYAL SOCIETY A MATHEMATICAL, PHYSICAL & ENGINEERING SCIENCES

most rapidly in the vacuum exterior above the pole. A $t =$ const. slice has a spatial metric

$$ds^2 = A^2\,dr^2 + A^2 r^2\,d\theta^2 + B^2 r^2 \sin^2\theta\,d\phi^2.$$

In flat space $A = B = 1$. At the termination of the simulation these quantities have a modest maximum value $A \approx B \approx 1.7$, which occurs at the origin. They decrease monotonically outwards, reaching unity at large distances. However, it is their second derivatives that contribute to I and these blow up. While A and B steadily grow with time, I diverges much more rapidly. The behaviour is similar to the logarithmic divergence of the metric in the analytic prolate sequence of Nakamura *et al.* (1988). We emphasize that the above characterization of the singularity and the behaviour of the metric is dependent on the time slicing and may be different for other choices of time coordinate. In principle the spindle singularity might first occur at the centre rather than the pole with a different time slicing.

The absence of an apparent horizon does not necessarily imply the absence of a global event horizon, although the converse is true. Recently Wald & Iyer (1991) have emphasized this point by showing that even Schwarzschild space-time can be sliced with non-spherical slices that approach arbitrarily close to the singularity without any trapped surfaces. Because such singularities cause our numerical integrations to terminate, we cannot map out a space-time arbitrarily far into the future, which would be necessary to completely rule out the formation of an event horizon. However, we do not think this is at all likely: for collapse from an initially compact state (figure 11), outward null geodesics turn around near the singularity. For collapse from large radius, by contrast (figure 12), outward null geodesics are still propagating freely away from the vicinity of the singularity up to the time our integrations terminate. It is an interesting question for future research whether any time slicing can be found which will be more effective in snuggling up to the singularity without actually hitting it. Such a slicing would enable one to confirm that all outward null geodesics propagate to large distances.

(Maximal slicing apparently does not hold back the formation of prolate spindle singularities. For prolate spheroids the newtonian potential diverges only logarithmically as the eccentricity $\to 1$, which may explain why α does not plummet precipitously near a spindle.)

Further evidence for the nakedness of the singularity is the similarity of the spindle singularity to the infinite cylinder naked singularity. In both cases the proper length of a given segment of matter along the axis grows slowly, while its proper circumference and surface area shrink to zero much more rapidly. Also, the singularity is an extended region along the axis and not just a point.

We have also followed the collapse of an initially oblate configuration with the same initial eccentricity and semi-major axis as figure 12. Following pancaking, it overshoots, becomes prolate and forms a black hole. At the time our integrations terminate, we find that $\mathscr{C}^{\min}_{\text{pole}} = \mathscr{C}^{\min}_{\text{eq}} = 0.85\ (4\pi M)$.

All of the above results are consistent with the hoop conjecture. When black holes form, the minimum polar and equatorial circumferences satisfy $\mathscr{C}^{\min} \lesssim 4\pi M$. Conversely, when naked singularities form the minimum polar circumference is much bigger than this value. In all cases where an apparent horizon forms, its area satisfies to within numerical accuracy $\mathscr{A} \leqslant 16\pi M^2$, as required theoretically. In every case we find that gravitational radiation carries away a negligible fraction ($\ll 1\,\%$) of the total mass-energy by the time a black hole or naked singularity forms.

PHILOSOPHICAL TRANSACTIONS OF THE ROYAL SOCIETY A MATHEMATICAL, PHYSICAL & ENGINEERING SCIENCES

(*d*) *Conclusions*

We have presented numerical evidence that the hoop conjecture is a valid criterion for the formation of black holes during non-spherical gravitational collapse. We have also found numerical candidates for the formation of naked singularities from non-singular initial configurations. These examples are in contrast with any case of singularities which may arise during spherical collapse. There the exterior space-time is always the Schwarzschild metric and the Riemann invariant is always exactly $48M^2/r_s^6$, which is finite outside the matter. In spherical collapse the singularities can thus only occur inside the matter. Here the singularities extend above the pole into the vacuum exterior. These examples suggest that the unqualified cosmic censorship hypothesis cannot be valid.

While the matter treated here has kinetic pressure, it is collisionless, not fluid. We do not regard the collisional properties of the matter as crucial. First, the formation of naked singularities should not depend on the particular details of the fundamental interactions affecting matter at high densities. The gravitational field equations alone should be sufficient to rule out naked singularities, at least in the vacuum exterior, for true cosmic censorship. Second, collisional effects may even accelerate the formation of singularities via relativistic 'pressure regeneration' (Misner *et al.* 1973). There is at least one tentative numerical example of prolate fluid collapse (adiabatic index $\Gamma \to 2$) that appears to be evolving to a singular state without the formation of an apparent horizon (Nakamura & Sato 1982; Nakamura *et al.* 1987).

It is not impossible that naked singularities qualitatively similar to the ones here may even arise in vacuum space-times. Since the sequence of momentarily static spheroids (Nakamura *et al.* 1988) proved to be a predictor of the singularities found in the dynamical calculations, we have been motivated to seek similar sequences of pure vacuum initial data. We have constructed two sequences characterized by long prolate concentrations of mass-energy: linear strings of black holes, and Brill waves with characteristic widths much less than their lengths. We find once again that the surrounding gravitational tidal field diverges for limiting members of these sequences, but that no apparent horizons occur when the configurations are sufficiently long. It would be interesting to use these solutions as initial data in dynamical evolutions.

The collisionless matter simulations described so far have no angular momentum. The presence of angular momentum could prevent an infinitesimally thin spindle singularity from forming on the axis. Recently, Apostolatos & Thorne (1992) have shown that, as in newtonian theory, an infinitesimal amount of rotation is sufficient to prevent the formation of a singularity in the relativistic collapse of an infinite dust cylinder. This still leaves open the possibility that collapsing configurations of finite size can still collapse to singularities in the presence of rotation. Recall that a small amount of angular momentum does not prevent the formation of a singularity when a Kerr black hole forms.

To explore this question, we have recently used our code to study the collapse of rotating collisionless spheroids (Shapiro & Teukolsky 1992). The spheroids are initially prolate and consist of equal numbers of co- and counter-rotating particles, as in the infinite case treated by Apostolatos & Thorne (1992). Although individual particles are rotating, the spheroid has no net angular momentum. This restriction greatly simplifies the space-time: the metric still has the same form as equation (11.1). We find that rotation significantly modifies the evolution when it is

PHILOSOPHICAL TRANSACTIONS OF THE ROYAL SOCIETY A MATHEMATICAL, PHYSICAL & ENGINEERING SCIENCES

sufficiently large. Imploding configurations with appreciable rotation ultimately collapse to black holes. However, for small enough angular momentum, our simulations cannot at present distinguish rotating from non-rotating collapse: spindle singularities appear to arise without apparent horizons. Hence it is possible that even spheroids with some angular momentum may form naked singularities.

Appendix A

Here we list the key equations for the evolution of an axisymmetric configuration in the ADM 3+1 decomposition of general relativity. We specialize to the case of no net angular momentum (Evans 1984). We adopt the space-time coordinates (t, r, θ, ϕ). Because of axisymmetry all quantities are functions only of (t, r, θ).

The metric is given by equation (11.1). In addition to the metric coefficients α, β^r, β^θ, A and B, the ADM formalism introduces the components of the extrinsic curvature tensor, $K^i{}_j$. It is convenient to introduce the related quantities

$$\hat{K}^i{}_j \equiv A^2 B K^i{}_j. \tag{A 1}$$

The evolution equations, which we use to determine the 'radiation variables' $\eta = \ln(A/B)$ and $\hat{K}^r{}_\theta$, are:

$$\partial_t \eta = (\alpha/A^2B)\,\hat{\lambda} + \beta^r \partial_r \eta + \beta^\theta \partial_\theta \eta + \partial_\theta \beta^\theta - \beta^\theta \cot\theta, \tag{A 2}$$

$$\begin{aligned}\partial_t \hat{K}^r{}_\theta = {} & (1/r^2)\,\partial_r (r^2 \beta^r \hat{K}^r{}_\theta) + (1/\sin\theta)\,\partial_\theta (\sin\theta\, \beta^\theta \hat{K}^r{}_\theta) \\ & - \frac{\alpha A}{r \sin\theta}\left\{\partial_\theta\left[\frac{\sin\theta}{A}\partial_r (Br)\right] - \frac{1}{A^2}\partial_r (Ar)\,\partial_\theta (B\sin\theta)\right\} \\ & + \hat{K}^r{}_\theta (\partial_\theta \beta^\theta - \partial_r \beta^r) + (2\hat{\lambda} - 3\hat{K}^\phi{}_\phi)\,\partial_\theta \beta^r - AB\,\partial_\theta (A^{-1}\partial_r \alpha) \\ & + (B/Ar)\,\partial_r (Ar)\,\partial_\theta \alpha - (\alpha/A^2)\,S_{r\theta},\end{aligned} \tag{A 3}$$

where

$$\hat{\lambda} = \hat{K}^r{}_r + 2\hat{K}^\phi{}_\phi$$

and where matter source terms like $S_{r\theta}$ will be defined below.

The momentum constraint equations, which we use to solve for $\hat{K}^r{}_r$ and $\hat{K}^\phi{}_\phi$, are

$$\frac{1}{\sin\theta}\partial_\theta (\sin\theta \hat{K}^r{}_r) + \frac{T}{\sin^2\theta}\partial_\theta\left(\frac{\sin^2\theta}{T}\hat{K}^\phi{}_\phi\right) = -S_\theta + \frac{1}{r^2}\partial_r (r^2 \hat{K}^r{}_\theta), \tag{A 4}$$

$$r^{-3}\partial_r (r^3 \hat{K}^r{}_r) + \hat{K}^\phi{}_\phi \partial_r \eta = S_r - (1/r^2 \sin\theta)\,\partial_\theta (\sin\theta\, \hat{K}^r{}_\phi), \tag{A 5}$$

where $T = A/B$. The hamiltonian constraint equation determines $\psi = B^{\frac{1}{2}}$:

$$\begin{aligned}r^{-2}\partial_r (r^2 \partial_r \psi) + (1/r^2 \sin\theta)\,\partial_\theta (\sin\theta\, \partial_\theta \psi) = {} & -\tfrac{1}{4}\psi[r^{-1}\partial_r (r\,\partial_r \eta) + r^{-2}\partial_\theta^2 \eta \\ & + (1/T^2\psi^8)\{\hat{\lambda}^2 - 3\hat{\lambda}\hat{K}^\phi{}_\phi + 3(\hat{K}^\phi{}_\phi)^2 + (\hat{K}^r{}_\theta/r)^2\}] - \rho^*/4\psi.\end{aligned} \tag{A 6}$$

To impose the maximal slicing condition on the time coordinate, we solve the 'lapse' equation for α

$$\begin{aligned}r^{-2}\partial_r [r^2 \partial_r (\alpha\psi)] + (1/r^2 \sin\theta)\,\partial_\theta [\sin\theta\, \partial_\theta (\alpha\psi)] = {} & \tfrac{1}{4}\alpha\psi[-r^{-1}\partial_r (r\,\partial_r \eta) - r^{-2}\partial_\theta^2 \eta \\ & + (7/A^2B^2)\{\hat{\lambda}^2 - 3\hat{\lambda}\hat{K}^\phi{}_\phi + 3(\hat{K}^\phi{}_\phi)^2 + (\hat{K}^r{}_\theta/r)^2\} + B^{-1}(\rho^* + 2S)].\end{aligned} \tag{A 7}$$

Imposing isotropic spatial coordinates leads to the 'shift' equations for β^r and β^θ:

$$r\,\partial_r (\beta^r/r) - \partial_\theta \beta^\theta = (\alpha/A^2B)\,(2\hat{\lambda} - 3\hat{K}^\phi{}_\phi), \tag{A 8}$$

$$r\,\partial_r \beta^\theta + \partial_\theta (\beta^r/r) = (2\alpha/A^2 Br)\,\hat{K}^r{}_\theta. \tag{A 9}$$

The geodesic equations of motion for the collisionless particles are:

$$\mathrm{d}r/\mathrm{d}t = \alpha u_r/\hat{u}A^2 - \beta^r, \tag{A 10}$$

$$\mathrm{d}\theta/\mathrm{d}t = \alpha u_\theta/\hat{u}A^2 r^2 - \beta^\theta, \tag{A 11}$$

$$\mathrm{d}\phi/\mathrm{d}t = (\alpha/B^2 r^2 \sin^2\theta)\, u_\phi/\hat{u}, \tag{A 12}$$

$$\mathrm{d}u_r/\mathrm{d}t = -\hat{u}\,\partial_r \alpha + u_r\,\partial_r \beta^r + u_\theta\,\partial_r \beta^\theta - \frac{\alpha}{2\hat{u}}\left[\partial_r\left(\frac{1}{A^2}\right)u_r{}^2 + \partial_r\left(\frac{1}{r^2 A^2}\right)u_\theta{}^2 + \partial_r\left(\frac{1}{B^2 r^2}\right)\frac{u_\phi{}^2}{\sin^2\theta}\right], \tag{A 13}$$

$$\mathrm{d}u_\theta/\mathrm{d}t = -\hat{u}\,\partial_\theta \alpha + u_r\,\partial_\theta \beta^r + u_\theta\,\partial_\theta \beta^\theta - \frac{\alpha}{2\hat{u}}\left[\partial_\theta\left(\frac{1}{A^2}\right)u_r{}^2 + \partial_\theta\left(\frac{1}{r^2 A^2}\right)u_\theta{}^2 + \partial_\theta\left(\frac{1}{B^2 r^2 \sin^2\theta}\right)u_\phi{}^2\right], \tag{A 14}$$

$$\mathrm{d}u_\phi/\mathrm{d}t = 0, \tag{A 15}$$

where the normalization condition $u^\mu u_\mu = -1$ gives

$$\hat{u} \equiv \alpha u^0 = \left[1 + \frac{u_r{}^2}{A^2} + \frac{u_\theta{}^2}{r^2 A^2} + \frac{u_\phi{}^2}{B^2 r^2 \sin^2\theta}\right]^{\frac{1}{2}}. \tag{A 16}$$

The particles are binned to determine the source terms for the field equations:

$$\rho^* = \sum_j \frac{m\hat{u}_j}{(r^2 \sin\theta\, \Delta r\, \Delta\theta\, \Delta\phi)_j}, \tag{A 17}$$

$$S_r = \sum_j \frac{m u_r^j}{(r^2 \sin\theta\, \Delta r\, \Delta\theta\, \Delta\phi)_j}, \tag{A 18}$$

$$S_\theta = \sum_j \frac{m u_\theta^j}{(r^2 \sin\theta\, \Delta r\, \Delta\theta\, \Delta\phi)_j}, \tag{A 19}$$

$$S_{r\theta} = \sum_j \frac{m u_r^j u^j{}_\theta}{\hat{u}_j (r^2 \sin\theta\, \Delta r\, \Delta\theta\, \Delta\phi)_j}, \tag{A 20}$$

$$S = \rho^* - \sum_j \frac{m}{\hat{u}_j (r^2 \sin\theta\, \Delta r\, \Delta\theta\, \Delta\phi)_j}. \tag{A 21}$$

The Brill mass of the space-time is given at any instant by

$$M = \frac{1}{2\pi}\int \mathrm{d}^3 x \left[(\nabla \ln\psi)^2 + \hat{K}_{ij}\hat{K}^{ij}\left(\frac{1}{8A^2 B^2}\right) + \tfrac{1}{4}A^2 \rho^*\right], \tag{A 22}$$

where ∇ is the flat space gradient operator.

References

Apostolatos, T. A. & Thorne, K. S. 1992 *Phys. Rev.* D. (In the press.)

Arnowitt, R., Deser, S. & Misner, C. W. 1962 In *Gravitation: an introduction to current research* (ed. L. Witten), p. 227. New York: John Wiley.

Bardeen, J. M. & Piran, T. 1983 *Phys. Rep.* **96**, 205.

Begelman, M. C., Blandford, R. D. & Rees, M. J. 1984 *Rev. mod. Phys.* **56**, 255.

Bisnovatyi-Kogan, G. S. & Thorne, K. S. 1970 *Astrophys. J.* **160**, 875.

Bisnovatyi-Kogan, G. S. & Zel'dovich, Ya. B. 1969 *Astrofizika*, **5**, 223.
Einstein, A. 1939 *Ann. Math.* **40**, 922.
Evans, C. R. 1984 Ph.D. thesis, University of Texas at Austin.
Fackerell, E. D. 1968 *Astrophys. J.* **153**, 643.
Fackerell, E. D. 1970 *Astrophys. J.* **160**, 859.
Fackerell, E. D., Ipser, J. R. & Thorne, K. S. 1969 *Comments Ap. Space Phys.* **1**, 134.
Goldwirth, D. S., Ori, A. & Piran, T. 1989 In *Frontiers in numerical relativity* (ed. C. R. Evans, L. S. Finn & D. W. Hobill), p. 414. Cambridge University Press.
Ipser, J. R. 1969 *a* *Astrophys. J.* **156**, 509.
Ipser, J. R. 1969 *b* *Astrophys. J.* **158**, 17.
Ipser, J. R. 1980 *Astrophys. J.* **238**, 1101.
Ipser, J. R. & Thorne, K. S. 1968 *Astrophys. J.* **154**, 251.
Katz, J. & Horwitz, G. 1974 *Astrophys. J.* **194**, 439.
Kochanek, C. S., Shapiro, S. L. & Teukolsky, S. A. 1987 *Astrophys. J.* **320**, 73.
Lin, C. C., Mestel, L. & Shu, F. H. 1965 *Astrophys. J.* **142**, 1431.
Misner, C. W., Thorne, K. S. & Wheeler, J. A. 1973 *Gravitation*. San Francisco: Freeman.
Nakamura, T., Oohara, K. & Kojima, Y. 1987 *Prog. theor. Phys. Suppl.* **90**, 57.
Nakamura, T. & Sato, H. 1982 *Prog. theor. Phys.* **68**, 1396.
Nakamura, T., Shapiro, S. L. & Teukolsky, S. A. 1988 *Phys. Rev.* D **38**, 2972.
Penrose, R. 1969 *Rivista Nuovo Cim.* **1** (Numero Special), 252.
Petrich, L., Shapiro, S. L. & Teukolsky, S. A. 1985 *Phys. Rev.* D **31**, 2459.
Petrich, L., Shapiro, S. L. & Teukolsky, S. A. 1986 *Phys. Rev.* D **33**, 2100.
Quinlan, G. D. & Shapiro, S. L. 1987 *Astrophys. J.* **321**, 199.
Quinlan, G. D. & Shapiro, S. L. 1989 *Astrophys. J.* **343**, 725.
Quinlan, G. D. & Shapiro, S. L. 1990 *Astrophys. J.* **356**, 483.
Rasio, F. A., Shapiro, S. L. & Teukolsky, S. A. 1989 *a* *Astrophys. J. Lett.* **336**, L63.
Rasio, F. A., Shapiro, S. L. & Teukolsky, S. A. 1989 *b* *Astrophys. J.* **344**, 146.
Rees, M. J. 1984 *A. Rev. Astr. Astrophys.* **22**, 471.
Shapiro, S. L. & Teukolsky, S. A. 1985 *a* *Astrophys. J.* **298**, 34. (Paper I.)
Shapiro, S. L. & Teukolsky, S. A. 1985 *b* *Astrophys. J.* **298**, 58. (Paper II.)
Shapiro, S. L. & Teukolsky, S. A. 1985 *c* *Astrophys. J. Lett.* **292**, L41. (Paper III.)
Shapiro, S. L. & Teukolsky, S. A. 1986 *Astrophys. J.* **307**, 575. (Paper IV.)
Shapiro, S. L. & Teukolsky, S. A. 1987 *Astrophys. J.* **318**, 542.
Shapiro, S. L. & Teukolsky, S. A. 1988 *Science, Wash.* **241**, 421.
Shapiro, S. L. & Teukolsky, S. A. 1991 *a* *Phys. Rev. Lett.* **66**, 994.
Shapiro, S. L. & Teukolsky, S. A. 1991 *b* *Am. Sci.* **79**, 330.
Shapiro, S. L. & Teukolsky, S. A. 1992 *Phys. Rev.* D **45**, 2206.
Smarr, L. & York, J. W. 1978 *Phys. Rev.* D **17**, 1945.
Suffern, K. G. & Fackerell, E. D. 1976 *Astrophys. J.* **203**, 477.
Synge, J. L. 1934 *Trans. R. Soc. Canada III* **28**, 127.
Thorne, K. S. 1972 In *Magic without magic: John Archibald Wheeler* (ed. J. Klauder), p. 1. San Francisco: Freeman.
Wald, R. M. 1984 *General relativity*. University of Chicago Press.
Wald, R. M. & Iyer, V. 1991 *Phys. Rev.* D **44**, R3719.
Walker, A. G. 1936 *Proc. Edinb. math. Soc.* **4**, 238.
Zapolsky, H. S. 1968 *Astrophys. J. Lett.* **153**, L163.
Zel'dovich, Ya. B. & Novikov, I. D. 1971 *Relativistic astrophysics*, vol. 1. University of Chicago Press.
Zel'dovich, Ya. B. & Podurets, M. A. 1965 *Astron. Zh.* **42**, 963. (English translation in *Soviet Astr. A.J.* **9**, 742.)

PHILOSOPHICAL TRANSACTIONS OF THE ROYAL SOCIETY A MATHEMATICAL, PHYSICAL & ENGINEERING SCIENCES